

A global model of intensity autocorrelation to determine laser pulse duration

Yufei Peng(彭雨菲), Liqiang Liu(刘励强), Lihong Hong(洪丽红), and Zhiyuan Li(李志远)

Citation: Chin. Phys. B, 2024, 33 (**5**): 054207. DOI: 10.1088/1674-1056/ad1c57
Journal homepage: http://cpb.iphy.ac.cn; http://iopscience.iop.org/cpb

What follows is a list of articles you may be interested in

Yb:CaF_2–YF_3 transparent ceramics ultrafast laser at dual gain lines

Xiao-Qin Liu(刘晓琴), Qian-Qian Hao(郝倩倩), Jie Liu(刘杰), Dan-Hua Liu(刘丹华), Wei-Wei Li(李威威), and Liang-Bi Su(苏良碧)
Chin. Phys. B, 2022, 31 (**11**): 114205. DOI: 10.1088/1674-1056/ac720f

Carboxyl graphene oxide solution saturable absorber for femtosecond mode-locked erbium-doped fiber laser

Rui-dong Lv(吕瑞东), Lu Li(李璐), Yong-gang Wang(王勇刚), Zhen-dong Chen(陈振东), Si-cong Liu(刘思聪), Xi Wang(王茜), Jiang Wang(王江), Yong-fang Li(李永放)
Chin. Phys. B, 2018, 27 (**11**): 114214. DOI: 10.1088/1674-1056/27/11/114214

Observation of wavelength-switchable solitons in an all-polarization-maintaining erbium-doped fiber cavity based on graphene saturable absorber reflector

Kuo Meng(孟阔), Lian-Qing Zhu(祝连庆), Fei Luo(骆飞)
Chin. Phys. B, 2017, 26 (**1**): 014205. DOI: 10.1088/1674-1056/26/1/014205

Ultrafast population transfer in a Λ-configuration level system driven by few-cycle laser pulses

Zhang Wen-Jing (张文静), Xie Xiao-Tao (谢小涛), Jin Lu-Ling (金璐玲), Bai Jin-Tao (白晋涛)
Chin. Phys. B, 2013, 22 (**11**): 114210. DOI: 10.1088/1674-1056/22/11/114210

Shaping of few-cycle laser pulses via a subwavelength structure

Guo Liang (郭亮), Xie Xiao-Tao (谢小涛), Zhan Zhi-Ming (詹志明)
Chin. Phys. B, 2013, 22 (**9**): 094212. DOI: 10.1088/1674-1056/22/9/094212

A global model of intensity autocorrelation to determine laser pulse duration

Yufei Peng(彭雨菲), Liqiang Liu(刘励强), Lihong Hong(洪丽红), and Zhiyuan Li(李志远)†

School of Physics and Optoelectronics, South China University of Technology, Guangzhou 510640, *China*

(Received 1 September 2023; revised manuscript received 24 November 2023; accepted manuscript online 9 January 2024)

We present a new global model of collinear autocorrelation based on second harmonic generation nonlinearity. The model is rigorously derived from the nonlinear coupled wave equation specific to the autocorrelation measurement configuration, without requiring a specific form of the incident pulse function. A rigorous solution of the nonlinear coupled wave equation is obtained in the time domain and expressed in a general analytical form. The global model fully accounts for the nonlinear interaction and propagation effects within nonlinear crystals, which are not captured by the classical local model. To assess the performance of the global model compared to the classic local model, we investigate the autocorrelation signals obtained from both models for different incident pulse waveforms and different full-widthes at half-maximum (FWHMs). When the incident pulse waveform is Lorentzian with an FWHM of 200 fs, the global model predicts an autocorrelation signal FWHM of 399.9 fs, while the classic local model predicts an FWHM of 331.4 fs. The difference between the two models is 68.6 fs, corresponding to an error of 17.2%. Similarly, for a sech-type incident pulse with an FWHM of 200 fs, the global model predicts an autocorrelation signal FWHM of 343.9 fs, while the local model predicts an FWHM of 308.8 fs. The difference between the two models is 35.1 fs, with an error of 10.2%. We further examine the behavior of the models for Lorentzian pulses with FWHMs of 100 fs, 200 fs and 500 fs. The differences between the global and local models are 17.1 fs, 68.6 fs and 86.0 fs, respectively, with errors approximately around 17%. These comparative analyses clearly demonstrate the superior accuracy of the global model in intensity autocorrelation modeling.

Keywords: intensity autocorrelation, global model, ultrashort pulses, pulse-width measurement

PACS: 42.65.–k, 42.65.Ky, 42.65.Re **DOI:** 10.1088/1674-1056/ad1c57

1. Introduction

The field of ultrafast optics has witnessed remarkable advancements over the past half century, spanning the nanosecond (ns), picosecond (ps), femtosecond (fs) and attosecond (as) time scales.[1–3] The introduction of chirped pulse amplification (CPA) by Mourou *et al.* in the 1980s revolutionized ultrafast, high-intensity lasers,[4,5] enabling tera-Watt (TW, 10^{12} W) power outputs without damaging optical elements.[6] Amplified ultrafast lasers have since become indispensable tools for studying ultrafast phenomena and finding applications in various scientific and industrial domains, including microscopy,[7] spectroscopy[8,9] and high-precision material processing.[10,11] Since the temporal resolution requirements in ultrafast research surpass the capabilities of traditional photodetectors and oscilloscopes, the development of accurate measurement methods for ultrafast pulses becomes crucial. Over the years, numerous techniques for ultrafast laser pulse characterization have been proposed,[12–17] each offering distinct features suitable for specific conditions. Among these techniques, intensity autocorrelation[18,19] stands out as a widely used tool for its simplicity in experimental implementation, providing a measurement of the pulse duration without requiring phase information. In the 1990s, frequency-resolved optical gating (FROG)[12,13] and spectral phase interferometry for direct electric-field reconstruction (SPIDER)[14,15] were introduced as leading techniques for full pulse characterization, enabling the reconstruction of both the pulse amplitude and phase. However, these methods have not been rigorously derived from fundamental optical physics, in particular, nonlinear optics theory. Traditionally, the autocorrelation signal has been expressed as the cross-correlation of two pulse replicas, neglecting the effects of pulse propagation through the nonlinear crystal medium.[20,21] This approach, referred to as the local model, oversimplifies the pulse dynamics. In this study, we present a new global model for intensity autocorrelation that is rigorously derived from the fundamental optical wave transport equation and incorporates nonlinear optics theory. Our global model takes into account the nonlinear optical effects of the medium, providing a more comprehensive and accurate description of the autocorrelation process. We demonstrate the advantages of our model by comparing it with the traditional local model, highlighting its ability to accurately predict and explain nonlinear optical phenomena. By incorporating the nonlinear theory into the intensity autocorrelation modeling, our approach enhances the understanding and characterization of ultrafast laser pulses, paving the way for improved pulse optimization and control in a wide range of laser science and technology applications.

†Corresponding author. E-mail: phzyli@scut.edu.cn

© 2024 Chinese Physical Society and IOP Publishing Ltd

2. Theory

The experimental setup for the intensity autocorrelator, widely adopted in the optics community, is depicted in Fig. 1. The pulse to be measured is split into a probe pulse and a replica using a beam splitter. The probe pulse is directly focused onto a second harmonic generation (SHG) beta barium borate (BBO) crystal thin plate. The replica pulse, on the other hand, is directed through a translation stage before being focused onto the crystal. By adjusting the time delay using the translation stage, the optical path of the replica pulse can be varied, resulting in different degrees of overlap between the two pulses at the BBO SHG crystal. Figure 2 schematically illustrates three different scenarios of pulse overlap as the probe and replica pulses propagate within the nonlinear crystal, generating an SHG signal pulse that grows and propagates alongside the fundamental wave (FW) pulses. This physical representation forms the foundation for the global model that will be extensively discussed in this study. The replica pulse serves as the gating pulse, scanning through the probe pulse as the time delay is changed. The z-axis, as illustrated in Fig. 1, corresponds to the direction of propagation within the experimental setup. The autocorrelator configuration is carefully chosen to ensure phase matching conditions are met, allowing significant SHG (or more accurately, degenerate sum-frequency generation, SFG) only when the two pulses overlap and phase matching is satisfied. As depicted in Fig. 2, no SHG signal is generated when the two incident pulses initially enter the crystal. As the pulses propagate through the crystal, the SHG pulse gradually emerges and intensifies.

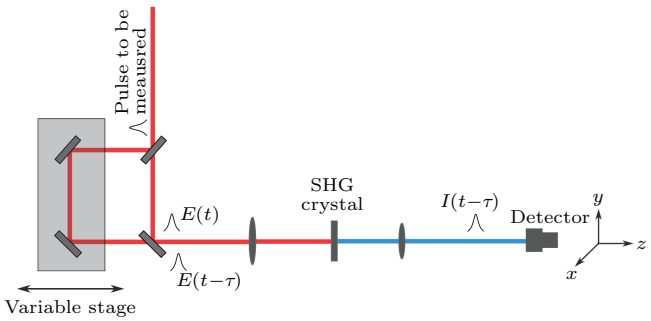


Fig. 1. Schematic diagram of the collinear autocorrelation.

We present the commonly used autocorrelation model and our new global model, including the theoretical derivations and calculation results to compare the differences. Before going into the details, it is worthwhile to present a simple picture of the autocorrelation measurement illustrated above. Note that this device works by correlating the SHG signal induced by the two pulses nonlinearly interacting with the BBO plate with delay τ of the gate pulse relative to the probe pulse. Then, in principle, it is necessary to accurately examine the pulse-pulse linear transport and nonlinear interaction detail and their contribution to the output SHG signal intensity. Previous works simply expressed the autocorrelation intensity as a cross-correlation

$$I_{\text{auto}}(\tau) \propto \int_{-\infty}^{+\infty} I(t)I(t-\tau)\,\mathrm{d}t. \tag{1}$$

Here, $I(t)$ is the intensity of the incident light pulse. Note that Eq. (1) is only a qualitative relation for determining the pulse width. However, this equation does not fully account for the nonlinear wave transport and interaction effects that occur during the second-order nonlinear process. It assumes that SHG signal generated in each position of BBO plate will simply add up algebraically without considering its phase retardation effect. Obviously, this is a local model of autocorrelation, which is subject to some certain approximation.

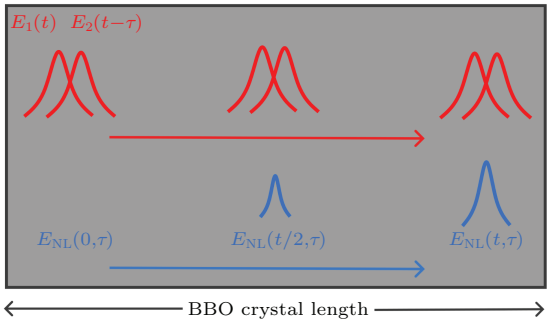


Fig. 2. Propagation of incident pulses and autocorrelation signal in the BBO crystal. The red pulses indicate two incident pulses and the blue pulse indicates the SHG pulse. The SHG pulse is gradually enhanced along the propagation distance inside the crystal.

In order to obtain a rigorous solution, we need to fully consider the local SHG signals excited across the whole BBO plate and their transport phase delay effect upon the geometric summation to create the final output SHG signal. This global model of autocorrelation starts from the nonlinear Maxwell's equation and the consequent wave equation that describe the wave propagation and the corresponding SHG process in the nonlinear medium:

$$\nabla^2 \boldsymbol{E}(\boldsymbol{r},t) = \mu_0\varepsilon_0\varepsilon\frac{\partial^2 \boldsymbol{E}(\boldsymbol{r},t)}{\partial t^2} + \mu_0\frac{\partial^2 \boldsymbol{P}(\boldsymbol{r},t)}{\partial t^2}, \tag{2}$$

where μ_0 is the magnetic permeability of free space, ε_0 is the electric permittivity of free space and ε is the material permittivity. $\boldsymbol{E}(\boldsymbol{r},t)$ can denote either the electric field of the incident pulse or the SHG signal pulse. The polarization $\boldsymbol{P}(\boldsymbol{r},t)$ consists of the linear and nonlinear polarizations

$$\boldsymbol{P}(\boldsymbol{r},t) = \boldsymbol{P}^{(1)}(\boldsymbol{r},t) + \boldsymbol{P}^{(2)}_{\text{NL}}(\boldsymbol{r},t) + \cdots. \tag{3}$$

In the time domain, the linear polarization is expressed as such a convolution

$$\boldsymbol{P}^{(1)}(\boldsymbol{r},t) = \varepsilon_0\int_{-\infty}^{+\infty}\chi^{(1)}(\boldsymbol{r},t-t')\boldsymbol{E}(\boldsymbol{r},t')\,\mathrm{d}t'. \tag{4}$$

However, for autocorrelation measurements in the picosecond and femtosecond regimes, the response time of the BBO crystal is much smaller than the pulse duration. Hence, it is reasonable to approximate the linear polarization, where the effective susceptibility χ_{eff} is directly multiplied by the electric field $\boldsymbol{E}(\boldsymbol{r},t)$

$$\boldsymbol{P}^{(1)}(\boldsymbol{r},t)=\varepsilon_0\chi_{\text{eff}}\boldsymbol{E}(\boldsymbol{r},t). \tag{5}$$

So, the linear and nonlinear polarizations are

$$\boldsymbol{P}_1^{(1)}(\boldsymbol{r},t)=\varepsilon_0\chi_{\text{eff}}\boldsymbol{E}_1(\boldsymbol{r},t), \tag{6}$$
$$\boldsymbol{P}_2^{(1)}(\boldsymbol{r},t)=\varepsilon_0\chi_{\text{eff}}\boldsymbol{E}_2(\boldsymbol{r},t), \tag{7}$$
$$\boldsymbol{P}_{\text{NL}}^{(2)}(\boldsymbol{r},t)=2\varepsilon_0\chi_{\text{eff}}^{(2)}\boldsymbol{E}_1(\boldsymbol{r},t)\boldsymbol{E}_2(\boldsymbol{r},t). \tag{8}$$

In the case of collinear SHG autocorrelation, where the probe pulse E_1 and the gate pulse E_2 propagate within the nonlinear crystal plate and undergo second-order nonlinear interaction, the slowly varying envelope approximation (SVEA) is applied to solve the nonlinear interaction. The SVEA allows the pulse electric fields to be expressed as the product of a slowly varying envelope function and a fast-oscillating sine carrier wave function, except for pulses as short as a few optical cycles. Hence, $\boldsymbol{E}_1$ and $\boldsymbol{E}_2$ are written as

$$\boldsymbol{E_1}(\boldsymbol{r},t)=\boldsymbol{E}_{\text{env},1}(\boldsymbol{r},t)\boldsymbol{E}_{\text{car},1}(\boldsymbol{r},t), \tag{9}$$
$$\boldsymbol{E_2}(\boldsymbol{r},t)=\boldsymbol{E}_{\text{env},2}(\boldsymbol{r},t-\tau)\boldsymbol{E}_{\text{car},2}(\boldsymbol{r},t). \tag{10}$$

Figures 1 and 2 illustrate the propagation of the two pulses along the z-axis. The incident pulse carrier wave is assumed to be monochromatic, with a frequency of ω and a wavenumber of k. The electric fields $\boldsymbol{E}_1$ and $\boldsymbol{E}_2$ can be expressed in the scalar form as

$$\begin{aligned}E_1(\boldsymbol{r},t)&=E_{\text{env},1}(z,t)E_{\text{car},1}(z,t)\\&=E_{\text{env},1}(z,t)\exp(-\mathrm{i}\omega_0 t+\mathrm{i}k_0 z),\end{aligned} \tag{11}$$
$$\begin{aligned}E_2(\boldsymbol{r},t)&=E_{\text{env},2}(z,t-\tau)E_{\text{car},2}(z,t)\\&=E_{\text{env},2}(z,t-\tau)\exp(-\mathrm{i}\omega_0 t+\mathrm{i}k_0 z).\end{aligned} \tag{12}$$

During the autocorrelation process, the resulting SHG pulse electric field E_{NL} is much weaker than the incident pulse, allowing for the use of the undepleted pump approximation. According to this approximation, the electric field of the pump wave is assumed to be constant over the propagation distance and the duration of the interaction. In scalar form we find

$$\begin{aligned}E_{\text{NL}}(\boldsymbol{r},t)&=E_{\text{env,NL}}(\boldsymbol{r},t)E_{\text{car,NL}}(\boldsymbol{r},t)\\&=E_{\text{env,NL}}(z,t)\exp(-\mathrm{i}2\omega_0 t+\mathrm{i}k_{\text{NL}}z).\end{aligned} \tag{13}$$

Since E_{NL} represents the sum frequency generation (SFG) of two incident pulses, its frequency is $2\omega_0$ and wavenumber is k_{NL}. Under the perfect matching condition, as in a usual autocorrelator instrument, we have $k_{\text{NL}}=2k_0$. Then,

$$E_{\text{NL}}(\boldsymbol{r},t)=E_{\text{env,NL}}(z,t)\exp(-\mathrm{i}2\omega_0 t+\mathrm{i}2k_0 z). \tag{14}$$

The induced second-order polarization becomes

$$\begin{aligned}P_{\text{NL}}^{(2)}(\boldsymbol{r},t)&=2\varepsilon_0\chi_{\text{eff}}^{(2)}\exp(-\mathrm{i}2\omega_0 t+2\mathrm{i}k_0 z)\\&\quad\times E_{\text{env},1}(z,t)E_{\text{env},2}(z,t-\tau).\end{aligned} \tag{15}$$

By assuming the validity of the SVEA, the higher-order derivatives can be neglected compared to the first-order derivatives, resulting in

$$\begin{aligned}\left|\frac{\partial^2 E_{\text{NL}}(\boldsymbol{r},t)}{\partial t^2}\right|&\ll\left|\omega\frac{\partial E_{\text{NL}}(\boldsymbol{r},t)}{\partial t}\right|,\\\left|\frac{\partial^2 E_{\text{NL}}(\boldsymbol{r},t)}{\partial z^2}\right|&\ll\left|k\frac{\partial E_{\text{NL}}(\boldsymbol{r},t)}{\partial z}\right|.\end{aligned} \tag{16}$$

Moreover, it is assumed that the nonlinear crystals used in autocorrelators are very thin and achieve perfect phase matching. Under these assumptions, Eq. (2) can be simplified as

$$\begin{aligned}&4\mathrm{i}k_z\frac{\partial E_{\text{env,NL}}(z,t)}{\partial z}+\frac{4\mathrm{i}\omega_0\varepsilon}{c^2}\frac{\partial E_{\text{env,NL}}(z,t)}{\partial t}\\&=-8\varepsilon_0\mu_0\omega_0^2\chi_{\text{eff}}^{(2)}E_{\text{env},1}(z,t)E_{\text{env},2}(z,t),\end{aligned} \tag{17}$$

where $\omega_0=ck_0$, $v=c/n$, $\varepsilon_0\mu_0=1/c^2$. n is the refractive index for the probe pulse. To further simplify the equation, the spatial coordinate is transformed to be centered on the pulse. The new coordinates, z' and t', are defined as $z'=z-vt$ and $t'=t$. Therefore, the derivatives in the new coordinate are

$$\begin{cases}\dfrac{\partial E_{\text{env,NL}}}{\partial z}=\dfrac{\partial E_{\text{env,NL}}}{\partial z'},\\[2ex]\dfrac{\partial E_{\text{env,NL}}}{\partial t}=-v\dfrac{\partial E_{\text{env,NL}}}{\partial z'}+\dfrac{\partial E_{\text{env,NL}}}{\partial t'}.\end{cases} \tag{18}$$

Replace them into Eq. (17) and we find

$$\begin{aligned}&\frac{\partial E_{\text{env,NL}}(z',t')}{\partial t'}\\&=(2\mathrm{i}k_0 v\chi_{\text{eff}}^{(2)}/n)E_{\text{env},1}\left(z',t'\right)E_{\text{env},2}\left(z',t'-\tau\right).\end{aligned} \tag{19}$$

Therefore, the SHG pulse can be described by

$$\begin{aligned}&E_{\text{env,NL}}(t,\tau)\\&=\frac{2\mathrm{i}k_0 v\chi_{\text{eff}}^{(2)}}{n}\int_{-\infty}^{t}E_{\text{env},1}\left(z',t'\right)E_{\text{env},2}\left(z',t'-\tau\right)\mathrm{d}t'.\end{aligned} \tag{20}$$

It is important to note that the above equation integrates over t'. The upper limit of the integral is t instead of infinity, as it accounts for the finite thickness of the BBO crystal used in this study, which is set at 50 μm. Consequently, the SHG pulse depends on both the temporal variable t and the delay τ. For each specific delay, we extract the maximum value from the signal-time curve. As a result, the variable t becomes irrelevant, and only the variable τ remains, representing the autocorrelation signal $E_{\text{env,NL}}(\tau)$. Until now, we have discussed the electric

field of the autocorrelation signal. The corresponding intensity can be calculated using

$$I_{\mathrm{NL}}(\tau) = \frac{1}{2}\varepsilon_0 c n_{2\omega_0} |E_{\mathrm{env,NL}}(\tau)|^2. \tag{21}$$

This equation represents a general form, where the incident pulse $E_{\mathrm{env},1}(z',t')$ can take on any shape or waveform. Equation (20) always indicates that the autocorrelation signal arises from the contribution of autocorrelation pulses up to the time t at the right end of the nonlinear crystal.

We assume three different waveforms for the incident pulse: Lorentzian, sech, and Gaussian. The corresponding incident electric field can be expressed as follows. For the Lorentzian pulse $E_1(t) = E_0/(1+\delta^2 t^2)$. For the sech pulse $E_1(t) = \mathrm{sech}(t/\delta) = E_0 \frac{2}{\mathrm{e}^{t/\delta} - \mathrm{e}^{-t/\delta}}$. For the Gaussian pulse $E_1(t) = E_0\,\mathrm{e}^{-2t^2/\delta^2}$. Here, t is the temporal variable, and δ is the pulse width parameter, which is adjusted to different incident pulse widths. The intensity $I(t)$ is defined by Eq. (21). In this study, we consider incident pulse widths of 100 fs, 200 fs and 500 fs as examples, with a single pulse energy on the order of tens of micro-Joules, which can be calculated by $\int I(t)\,\mathrm{d}t$. For the SHG process, the incident wavelength is set at 800 nm, resulting in a generated autocorrelation signal wavelength of 400 nm.

Once the properties of the incident pulse have been determined, the subsequent step involves calculating the autocorrelation signal in both models. This calculation primarily relies on Eqs. (1) and (20). It is worth noting that Eq. (1) is expressed as a positive correlation rather than an equation, which is a common representation of intensity autocorrelation signals in previous studies. Due to the undepleted pump approximation employed in the intensity autocorrelation case, the absolute value of the signal typically does not have a significant impact, leading to the omission of several coefficients. Therefore, expressing the positive correlation is a more rigorous approach than presenting it as an equation. Similarly, in our study, the signals in both models are normalized to ensure consistency. In the specific calculation process, we employ 480 discretized time units to describe the incident pulse. Each step covers a different time span based on the specific incident pulse width, ensuring a comprehensive depiction of the incident pulse. For the time delay, we utilize 320 discretized τ values in the numerical calculation. Similarly, the step size for τ is not constant but depends on the incident pulse width, enabling a complete representation of the signal trend. At each delay, the SHG signal is integrated over time, yielding a power value. This power-delay curve represents the autocorrelation signal of interest.

3. Results and discussion

To comprehensively evaluate the global model in comparison to the local model, we apply incident pulses with different waveforms and pulse widths to both models. Initially, we consider three commonly used waveforms in experiments: Lorentzian, sech, and Gaussian. Subsequently, we explore the influence of pulse width by employing incident pulses of the same waveform but with different pulse widths. Specifically, we utilize Lorentzian waveforms with pulse widths of 100 fs, 200 fs and 500 fs in this study. It is important to note that the calculation process in the local model is based on intensity, while in the global model, it is based on the electric field. When comparing the results of the two models, all outcomes are converted into intensities for consistency.

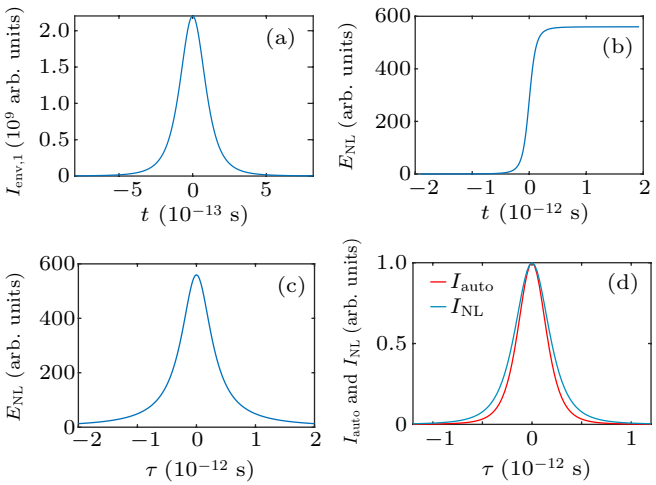


Fig. 3. Numerical calculations when the incident pulse is Lorentzian. (a) The incident pulse with 200.0 fs FWHM. (b) The electric field of the SHG pulse versus time when delay τ is zero. (c) The electric field of the autocorrelation signal versus delay. (d) The normalized intensity of the autocorrelation signal versus delay. The blue curve denotes the autocorrelation signal in the global model and the red curve denotes that in the local model.

We begin by examining the case of a Lorentzian incident pulse with an FWHM of 200 fs. Autocorrelation signals are calculated for both models, and the results are presented in Fig. 3. To facilitate a direct comparison of the autocorrelation signal FWHMs obtained from the two models, a normalization process is performed on both signals. The autocorrelation signal obtained from the global model is represented by the blue curve, while the red curve corresponds to the local model. As observed in the figure, a notable difference exists between the two curves. The autocorrelation signal FWHM obtained using the global model is found to be 399.9 fs, whereas the local model yields a value of 331.4 fs. There is a difference of 68.6 fs in the FWHM results between the two models, with an associated error of 17.2%. The significant difference in the autocorrelation signal FWHMs between the two models indicates that the global model captures additional complexities that are missed by the local model. The broader FWHM obtained from the global model suggests the presence of nonlinear wave transport and interaction effects, which the local model fails to account for adequately. In the local model, the autocorrelation signal is derived from a simple algebraic summation of signals generated at each point within the BBO

plate. However, it is important to recognize that the nonlinear interaction occurring within the crystal is considerably more intricate. The signals generated at different positions within the plate contain distinct phase information, leading to amplification (constructive interference of wave) or cancelation (destructive interference of wave) depending on the phase characteristics. The final SHG signal is the result of a geometric summation that takes into account these phase-dependent interactions. The global model comprehensively captures the intrinsic properties of the SHG interaction, accounting for the phase-dependent amplification or cancelation of signals across the entire BBO plate. These additional factors contribute to the broadening of the autocorrelation signal compared to the local model. Therefore, the global model provides a more accurate representation and description of the autocorrelation process, offering valuable insight into the underlying dynamics.

Next, we investigate the performance of the global and local models using an incident sech pulse with an FWHM of 200 fs. The calculation process follows a similar approach to the Lorentzian case, and only the incident pulse and the corresponding autocorrelation signal are presented in Fig. 4. As shown in the figure, the FWHM of the autocorrelation signal calculated by the global model is 343.9 fs and that calculated by the local model is 308.8 fs. This results in a difference of 35.1 fs in the FWHM between the two models, with an associated error of 10.2%. Once again, the superiority of the global model in accurately describing the pulse dynamics is evident. By considering the nonlinear effects and incorporating the appropriate mathematical framework, the global model provides a more accurate representation and description of the autocorrelation signal, overcoming the limitations of the local model.

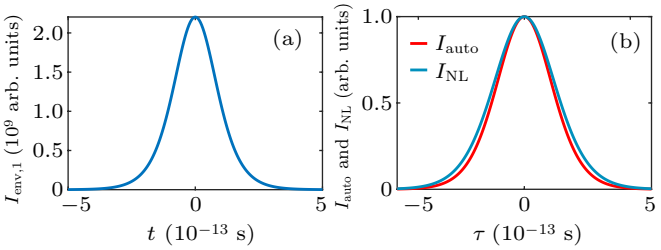


Fig. 4. Numerical calculations when the incident pulse is sech type. (a) The incident pulse with 200 fs FWHM. (b) The normalized intensity of the autocorrelation signal versus delay. The blue curve denotes the autocorrelation signal in the global model and the red curve denotes that in the local model.

In contrast to the Lorentzian and sech pulses, both the global and local models yield identical values for the autocorrelation signal FWHM when considering a Gaussian incident pulse with an FWHM of 200 fs. The autocorrelation signals obtained from both models exhibit an FWHM value of 282.8 fs. This intriguing observation can be attributed to the mathematical properties of the Gaussian function. Upon examining the equations derived from the global and local models, it becomes apparent that the difference between the two equations primarily lies in the order of squares and integrals. However, when substituting the Gaussian pulse into these equations, the order of squares and integrals has no effect due to the unique characteristics of the Gaussian function. Consequently, both models yield the same FWHM value for the autocorrelation signal. Nevertheless, this particularity is not present when considering incident pulses of other types, such as Lorentzian and sech. It is worth noting that the global and local models produce different results for Lorentzian and sech pulses, but yield the same results for a Gaussian pulse. Therefore, the discrepancy in FWHM between the two models depends on the waveform and width of the incident pulse.

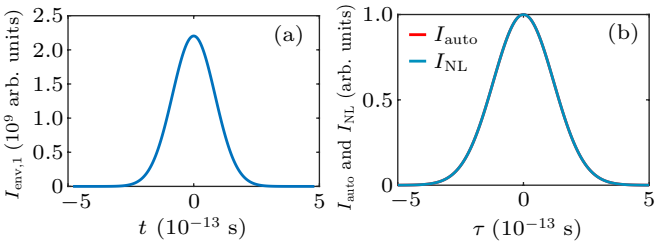


Fig. 5. Numerical calculations when the incident pulse is Gaussian. (a) The incident with 200 fs FWHM. (b) The normalized intensity of the autocorrelation signal versus delay. The blue curve denotes the autocorrelation signal in the global model and the red curve denotes that in the local model.

To further assess the robustness of the global model, we investigate scenarios involving incident pulses with different FWHMs. In addition to the previously discussed case of a 200 fs incident pulse, we introduce two more cases with Lorentzian incident pulses of 100 fs and 500 fs FWHMs. The results are presented in Fig. 6. It is evident that the red and blue curves do not overlap in either case, indicating a noticeable difference between the autocorrelation signals obtained from the global and local models. When the incident pulse has an FWHM of 100 fs, the global model calculates an autocorrelation signal FWHM of 99.9 fs, while the local model yields a value of 82.7 fs. This results in a difference of 17.1 fs in the FWHM between the two models, with an associated error of 17.1%. Similarly, for the incident pulse with an FWHM of 500 fs, the global model calculates an autocorrelation signal FWHM of 499.8 fs, whereas the local model yields a value of 413.9 fs. The difference in FWHM between the two models is 86.0 fs, with an error of 17.2%. In all three cases, significant discrepancies are observed between the autocorrelation signals obtained from the global and local models, and the error remains consistently around 17%. This consistency arises due to certain assumptions made by the global model, particularly the assumption of perfect phase matching. It is well known that phase mismatch can introduce various complications in the nonlinear process and lead to distorted signals. However, phase-related issues are typically not considered in intensity autocorrelation analysis, as it is a simplified method. As a result, neither the local nor the global model addresses complex

phase problems. This explains why the error remains roughly the same when the incident pulse waveform is the same.

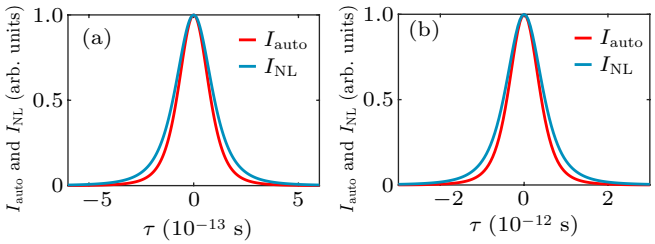


Fig. 6. Normalized autocorrelation signals of two models when the incident pulse is Lorentzian with different FWHMs. The blue curve denotes the autocorrelation signal in the global model and the red curve denotes that in the local model. (a) The autocorrelation signals when the incident pulse is 100 fs. (b) The autocorrelation signals when the incident pulse is 500 fs.

4. Conclusion

In summary, we have introduced a global model for intensity autocorrelation, providing a theoretical framework to accurately determine laser pulse duration. Through a comparative analysis with the traditional local model, we have demonstrated the superior accuracy and comprehensive nature of the global model. The global model, derived from the Maxwell equation within the framework of nonlinear theory, offers a more robust description of pulse dynamics and the resulting autocorrelation signal characteristics.

Our investigation has encompassed incident pulses with different waveforms and pulse widths. For incident pulses with a width of 200.0 fs, we have observed notable differences between the global and local models. In the case of a Lorentzian incident pulse, the global model calculated an autocorrelation signal FWHM of 399.9 fs, while the local model yielded a value of 331.4 fs. This results in a difference of 68.6 fs and an error of 17.2%. Similarly, for a sech incident pulse, the global model produces an autocorrelation signal FWHM of 343.9 fs, while the local model obtains a value of 308.8 fs. The difference between the two models is 35.1 fs with an error of 10.2%. Notably, for a Gaussian incident pulse, both models yield identical autocorrelation signals, which can be attributed to the mathematical properties of the Gaussian function.

Furthermore, we have explored the impact of pulse width factors by considering Lorentzian incident pulses with widths of 100 fs and 500 fs. In the case of a 100 fs incident pulse, the global model predicts an autocorrelation FWHM of 99.9 fs, while the local model yields a value of 82.7 fs. This results in a difference of 17.1 fs with an error of 17.1%. Similarly, for a 500 fs incident pulse, the global model produces an autocorrelation FWHM of 499.8 fs, whereas the local model obtains a value of 413.9 fs. The difference between the two models is 86.0 fs with an error of 17.2%. Collectively, these results highlight that regardless of the incident pulse width, the global and local models yield different autocorrelation signals.

Through comparison of the autocorrelation signal FWHMs obtained from both models, significant differences are observed, indicating the limitations of the local model in capturing the nonlinear effects that contribute to pulse broadening. The global model has consistently demonstrated superior accuracy across various waveforms and pulse durations. Overall, the global model for intensity autocorrelation presents a significant advancement in accurately describing and predicting autocorrelation signal characteristics, enabling researchers to better characterize and optimize ultrafast laser pulses in various applications.

Acknowledgements

Project supported by the Science and Technology Project of Guangdong (Grant No. 2020B010190001), the National Natural Science Foundation of China (Grant No. 11974119), the Guangdong Innovative and Entrepreneurial Research Team Program (Grant No. 2016ZT06C594), and the National Key R&D Program of China (Grant No. 2018YFA0306200).

References

[1] Hendow S T and Shakir S A 2010 *Opt. Express* **18** 10188
[2] Cheng J, Perrie W, Sharp M, Edwardson S P, Semaltianos N G, Dearden G and Watkins K G 2009 *Appl. Phys. A* **95** 739
[3] Soong H K and Malta J B 2009 *American Journal of Ophthalmology* **147** 189
[4] Strickland D and Mourou G 1985 *Opt. Commun.* **55** 447
[5] Maine P, Strickland D, Bado P, Pessot M and Mourou G 1988 *IEEE Journal of Quantum Electronics* **24** 398
[6] Maine P and Mourou G 1988 *Opt. Lett.* **13** 467
[7] Nakane T, Kotecha A, Sente A, McMullan G, Masiulis S, Brown P M G E, Grigoras I T, Malinauskaite L, Malinauskas T, Miehling J, Uchański T, Yu L, Karia D, Pechnikova E V, de Jong E, Keizer J, Bischoff M, McCormack J, Tiemeijer P, Hardwick S W, Chirgadze D Y, Murshudov G, Aricescu A R and Scheres S H W 2020 *Nature* **587** 152
[8] Klimov V I, Ivanov S A, Nanda J, Achermann M, Bezel I, McGuire J A and Piryatinski A 2007 *Nature* **447** 441
[9] Engel G S, Calhoun T R, Read E L, Ahn T K, Mančal T, Cheng Y C, Blankenship R E and Fleming G R 2007 *Nature* **446** 782
[10] Davis K M, Miura K, Sugimoto N and Hirao K 1996 *Opt. Lett.* **21** 1729
[11] Deubel M, von Freymann G, Wegener M, Pereira S, Busch K and Soukoulis C M 2004 *Nat. Mater.* **3** 444
[12] Trebino R and Kane D J 1993 *J. Opt. Soc. Am. A* **10** 1101
[13] Kane D J and Trebino R 1993 *Opt. Lett.* **18** 823
[14] Iaconis C and Walmsley I A 1998 *Opt. Lett.* **23** 792
[15] Gallmann L, Sutter D H, Matuschek N, Steinmeyer G, Keller U, Iaconis C and Walmsley I A 1999 *Opt. Lett.* **24** 1314
[16] Akturk S, Kimmel M, O'Shea P and Trebino R 2003 *Opt. Express* **11** 491
[17] Bowlan P, Gabolde P, Shreenath A, McGresham K, Trebino R and Akturk S 2006 *Opt. Express* **14** 11892
[18] Weber H P 1967 *J. Appl. Phys.* **38** 2231
[19] Weber H P 1968 *J. Appl. Phys.* **39** 6041
[20] Diels J C M, Fontaine J J, McMichael I C and Simoni F 1985 *Appl. Opt.* **24** 1270
[21] Hirayama T and Sheik-Bahae M 2002 *Opt. Lett.* **27** 860